I&EC research
Industrial & Engineering Chemistry Research

pubs.acs.org/IECR
Article

Impact of the PiperION Anion Exchange Membrane Thickness on the Performance of a CO_2-to-HCOOH Three-Compartment Electrolyzer

Bastian Rutjens,* Konstantin von Foerster, Bernhard Schmid, Henning Weinrich, Sergio Sanz, Hermann Tempel, and Rüdiger-A. Eichel

Cite This: *Ind. Eng. Chem. Res.* 2024, 63, 3986−3996

Read Online

ACCESS | Metrics & More | Article Recommendations | Supporting Information

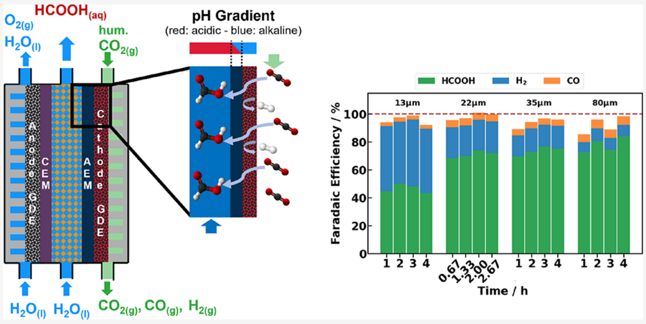

ABSTRACT: The electrochemical reduction of CO_2 to formic acid (HCOOH) is a sustainable synthetic approach with the potential to substitute for energy-demanding conventional processes. In this framework, the three-compartment electrolyzer presents a crucial technological advancement, facilitating the direct production of diluted HCOOH in the center compartment, which is separated from the anode and cathode by cation and anion exchange membranes (CEM and AEM), respectively. However, the impact of the AEM on both selectivity and energy consumption in the three-compartment electrolyzer remains largely unexplored. Herein, the use of PiperION AEMs, investigated under different thicknesses (13−80 μm), current densities (200−500 mA cm^{-2}), and center compartment flow rates (50−200 μL min^{-1}), confirms that the AEM acts as a barrier between the acidic center and the alkaline cathodic compartment. Thicker AEMs provide the optimal alkaline media in the cathode manifested by enhanced catalytic efficiency and selectivity (FE_{FA} up to 84%). The thinnest membrane (13 μm) yields diminished performance in terms of the faradaic efficiency of HCOOH, whereas the thickest membrane (80 μm) shows high cell voltages and limiting applicable current densities. However, medium thick membranes (22 and 35) present high faradaic efficiencies of HCOOH (FE_{FA} = 76%) with low specific energy consumptions (Q_{FA} = 5.9 kWh kg^{-1}) and increased HCOOH concentrations (c = 2.3 mol L^{-1}), given their enhanced shielding effects while maintaining moderate cell voltages (U = 3.8 V).

■ INTRODUCTION

To achieve sustainability in industry, it is imperative to mitigate CO_2 emissions or maintain a balance in input-output CO_2 fluxes during the transition from fossil fuels to environmentally friendly carbon sources.[1,2] CO_2 electroreduction to value-added products, with the possibility to couple them to renewable energy sources such as wind and solar power, is a promising approach contributing to this transformation.[3,4] The introduction of a cathodic catalyst in the process not only reduces the overall reaction potential but imparts specific selectivity for the final products, that is, CO, HCOOH, EtOH, and other C_{2+} derivatives.[4,5] Technological maturity with respect to these products is at different stages led by individual requirements and potential applications. For CO_2-to-CO electrolysis, scaling up and stacking into multiple cells are under investigation.[6−11] In contrast, the current focus for the CO_2-to-C_{2+} electrolysis focuses on the development of highly active and selective catalyst materials for application in batch reactors or single flow cells.[12−16] Selective and durable catalysts, particularly those based on bismuth and tin materials, have gained significant attention in the field of CO_2-to-HCOOH electroreduction. Moreover, their potential application in advanced electrolyzer configurations is of growing interest.[17−24]

HCOOH is of significant interest, not only as an important base chemical with several applications in the industry but also for its potential as an H_2 carrier and its utility in direct HCOOH fuel cells (DFAFCs).[25,26] Furthermore, recent studies indicate that the electrochemical production of HCOOH may become economically competitive to conventional synthesis routes, making it an economically viable and sustainable alternative.[27,28] However, most of the current electrolyzer setups in the literature produce $HCOO^-$, which needs to be converted into HCOOH via energy-intensive and wasteful processes.[29] This is avoided by the utilization of a three-compartment electrolyzer setup for direct production of

Received: December 15, 2023
Revised: February 11, 2024
Accepted: February 14, 2024
Published: February 22, 2024

https://doi.org/10.1021/acs.iecr.3c04459

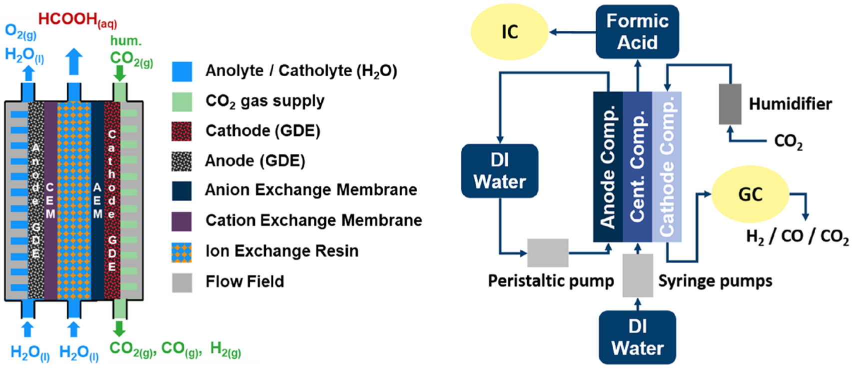

Figure 1. Illustration of direct HCOOH electrolyzer cell setup (left) and experimental liquid and gas flows (right).

HCOOH, such as the one investigated in this work, developed by researchers at Dioxide Materials, which combines the production of $HCOO^-$ and its protonation to HCOOH in a single cell.[18,30,31] Previous studies on this cell focused on evaluating the HCOOH production and examining the stability of the system over extended periods, with experiments spanning up to 1000 h, adding valuable insights into the electrochemical processes and efficiency.[18,30] Performance-enhancing modifications to the electrolyzer, such as the introduction of different solid electrolytes in the center compartment, have been demonstrated.[32,33] The cell setup has also been successfully tested for the electroreduction of CO_2-to-EtOH and other C_{2+} products using copper as a catalyst. This highlights the potential of the electrolyzer not only for HCOOH production but also for the synthesis of a broader range of compounds.[32,34,35] Theoretical analysis of the cell setup, including mass transport across different compartments, provided a deeper understanding of the ongoing process.[36]

Significant progress has been made in understanding and optimizing various aspects of direct HCOOH production; however, the investigation of the anion exchange membrane (AEM) as a crucial component of the cell concept has received little attention. Dioxide Materials proposes Sustainion as the AEM for this electrolyzer and has demonstrated stable operation with satisfactory performance in terms of faradaic efficiency and specific energy consumption of HCOOH.[18,30,37] Reports on other AEMs in different electrolyzer concepts proved promising results in CO_2 electroreduction to non-HCOOH products, due to their distinct membrane characteristics.[38−40] However, the influence of AEMs on the performance of direct HCOOH production, aiming at both enhanced efficiency and stability, remains unexplored. PiperION AEMs hold promise due to their comparable carbonate conductance to Sustainion and successful application in a CO_2-to-CO electrolyzer using a zero-gap setup. It is worth noting that thinner PiperION membranes yielded higher partial current densities of CO compared to thicker ones at different cell voltages. Moreover, these membranes achieved a stable operation of approximately 100 h at a partial current density of 400 mA cm^{-2}.[41]

Motivated by this success, herein, the use of PiperION AEMs in direct electroreduction of CO_2 to HCOOH is reported for the first time. Specifically, the impact of the thickness of the PiperION membrane on the cathodic reaction environment in the three-compartment electrolyzer is investigated. For that purpose, various operating parameters, including current density and center compartment flow rate, are evaluated with respect to faradaic efficiency, concentration, and specific energy consumption for HCOOH. This evaluation takes into account different PiperION AEM thicknesses ranging from 13 to 80 μm.

EXPERIMENTAL SECTION

Preparation of the Gas Diffusion Electrodes (GDEs). Bi_2O_3 nanoparticle (60 mg, <100 nm, Sigma-Aldrich, USA) catalyst material, 60 mg of Vulcan XC72 (Cabot Corporation, USA) conductive additive, and 96 μL PiperION 5 wt % solution (Versogen, USA) binder were dispersed in 4.0 mL of EtOH using an ultrasonic bath for ∼1 h. Subsequently, the resulting ink was spray-coated onto a carbon fiber substrate (Toray Paper 120 (TGP-H-120), 30% wet-proofed) using an airbrush to obtain a catalyst loading of 3.7 ± 0.2 mg cm^{-2}.

Electrolyzer Setup. The three-compartment electrolyzer for direct HCOOH production used in this study was acquired from Dioxide Materials and powered by a PGSTAT302N (Metrohm, Germany) potentiostat. The flow cell has an active geometric electrode area of 5 cm^2.[30] At the anode compartment, commercial IrO_2-coated GDEs (Dioxide Materials, USA) were used for the oxygen evolution reaction (OER). The cation exchange membrane (CEM), which separated the anode from the center compartment, was a Nafion N324 (Ion Power GmbH, Germany). Amberlite IR-120 (Acros Organics, Belgium) was used as an ion-exchange resin in the center compartment. PiperION membranes were chosen as AEMs (Versogen, USA) to separate the center compartment from the cathode. A schematic illustration of the cell assembly and gas and liquid flows is shown in Figure 1, left. Pictures of the inner components of the electrolyzer, that is, anode and cathode end plates with flow fields, gas diffusion electrodes, and center compartment are shown in Figure S2. AEMs were provided by the manufacturer in 13, 22, 35, and 80 μm thicknesses. Custom-made GDEs were employed as a cathode and were prepared as previously described. Peripheral arrangements delivered the necessary liquid and gaseous media to the cell and, in turn, collected the targeted HCOOH solution and gaseous CO and H_2 side products (Figure 1, right), as outlined in the following description: (a) A close-circuit of deionized water circulation (0.055 mS cm^{-1}) was provided by a peristaltic pump (Masterflex Reglo Miniflex Digital Pump, Ismatec, Germany) at the anode at a flow rate of 3 mL min^{-1}; (b) two syringe pumps (LA-100, Landgraf Laborsysteme, Germany) were used to provide a continuous flow of deionized water (0.055 mS cm^{-1}) to the center compartment at flow rates in the range of 50−200 μL min^{-1}; (c) the CO_2 feed

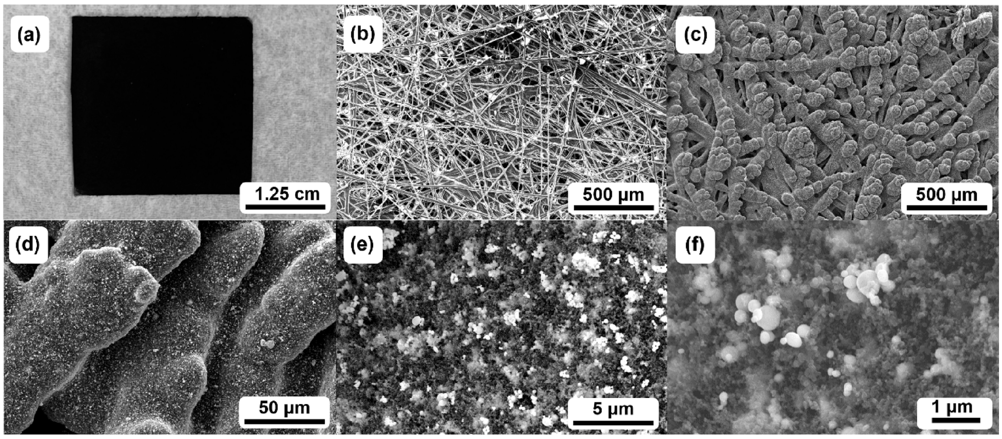

Figure 2. (a) Photo of a custom-made GDE as prepared. (b) SEM image of the carbon fiber substrate (Toray Paper (TGP-H-120), 30% wet-proofed). (c−f) SEM images of the custom-made GDE at different magnifications.

(99,995%, Air Products, Germany) at the cathode was humidified, with a water-filled bubbler, before entering the electrolyzer to prevent the AEMs from drying out and supplied in excess (60−150 mL min^{-1}, λ = constant) to ensure sufficient educt in the experiment; (d) liquid products coming out of the center compartment outlet were collected at time intervals and analyzed by ion exclusion chromatography (IC, S155, Sykam, Germany); (e) gaseous side products emerging from the cathode compartment outlet were analyzed using online gas chromatography (GC, Trace 1310, Thermo Fisher Scientific, Germany) and quantified via a drum gas counter (TG0.5−PP-PP, Ritter, Germany). Two parallel gas analyzer channels were used. Atmospheric gases and CO were separated using a 3 m × 1 mm column containing ShinCarbon ST with He carrier gas coupled to a thermal conductivity detector (TCD). H_2 was separated through a 2 m × 1 mm column packed with 5 Å molecular sieves with Ar carrier gas coupled to a TCD. Samples were injected from sample loops coupled directly to the experiment via a heated transfer line.

Measurement Procedure. The relationship between AEM thickness and electrolyzer performance was established by using a dedicated measurement procedure. For each experiment, a fresh custom-made cathode GDE and a PiperION AEM were employed. The procedure started with a ramp-up phase to ensure a stable operation after the assembly of the cell setup. Typically, chronoamperometry (CA) at 5 V was performed until a reasonable current of around 2.0−2.5 A was achieved. The first block of measurements, which evaluated the effect of the measuring time on the electrolyzer performance, started using chronopotentiometry (CP) at 200 mA cm^{-2} for ~4 h, a center compartment flow rate of 100 μL min^{-1}, and a CO_2 flow of 60 mL min^{-1}. Every hour, a liquid sample was acquired for IC analysis, and the volume of the accumulated liquid was determined. The second block of experiments explored the impact of the current density. Current densities of 500, 350, and 200 mA cm^{-2} were applied for an experimental time of 1 h. CO_2 flows were set to 150, 105, and 60 mL min^{-1} (corresponding to 500, 350, and 200 mA cm^{-2}, respectively) to maintain a stable CO_2 excess. The center compartment flow rate was maintained at 100 μL min^{-1}. The third block ascertained the impact of the center compartment flow rate. A constant current density of 200 mA cm^{-2} and a CO_2 supply of 60 mL min^{-1} were applied. The center compartment flow rate was set to 50, 100, and 200 μL min^{-1} lasting 1 h each. Liquid samples were acquired after 1 h and quantitatively analyzed. Throughout the entire procedure, side products originated at the outlet of the cathode were measured by online GC at ~15 min intervals. The fourth block studied the influence of the increased acidity in the center compartment on the faradaic efficiencies of HCOOH, H_2, and CO by the additional addition of 0, 0.924, 2.391, and 4.201 mol L^{-1} HCOOH solutions using a center compartment flow rate of 3 mL min^{-1}. Electrolysis was performed for 0.5 h for each concentration at current densities of 200, 350, and 500 mA cm^{-2}.

Utilizing the CP experimental data together with the concentrations determined by IC and GC measurements, the following key performance indicators (KPIs) were calculated using the equations below:

Faradaic efficiency of formic acid (FE_{FA}):

$$FE_{FA} = \frac{c_{FA}\cdot V}{n_{max}}\cdot 100\% = \frac{n_{FA}\cdot z\cdot F}{j\cdot A\cdot t}\cdot 100\% \tag{1}$$

Faradaic efficiency of gaseous side products, that is, FE_{H2} or FE_{CO}:

$$FE_{H2/CO} = \frac{z\cdot \dot{n}_{H2/CO}\cdot F}{j\cdot A}\cdot 100\% \tag{2}$$

Production rate of formic acid (P_{FA}):

$$P_{FA} = \frac{c_{FA}\cdot V}{A\cdot t} \tag{3}$$

Energy consumption of formic acid (Q_{FA}):

$$Q_{FA} = \frac{U\cdot q}{c_{FA}\cdot V\cdot M_{FA}} \tag{4}$$

Here, U denotes the cell voltage, j denotes the current density, and c denotes the avg. concentration, t denotes the elapsed time, V denotes the volume, A denotes the geometric active electrode area, M denotes the molar mass, n denotes the molar amount, q denotes the charge, z denotes the number of transferred electrons, F denotes the Faraday's constant, and $\dot{n}$ denotes the molar flow.

Related Electrochemical and Chemical Equilibria. At the cathode, CO_2 undergoes electrochemical reduction to $HCOO^-$, CO, and OH^- (reactions 5 and 6).[42,43] Additionally, the hydrogen evolution reaction (HER) takes place as a competing reaction (reaction 7). At the anode, the oxygen evolution reaction (OER, reaction 8) occurs, producing O_2 and protons.[42−44]

Cathode:

$$CO_2 + H_2O + 2e^- \quad E^0 = -0.48 \text{ V (vs. NHE)} \rightarrow HCOO^- + OH^- \tag{5}$$

$$CO_2 + H_2O + 2e^- \quad E^0 = -0.53 \text{ V(vs. NHE)} \rightarrow CO + 2OH^- \tag{6}$$

$$2H_2O + 2e^- \rightarrow 2OH^- + H_2 \quad E^0 = 0.00\text{V(vs. NHE)} \tag{7}$$

Anode:

$$2H_2O \rightarrow 4H^+ + 4e^- + O_2 \quad E^0 = +1.23\text{(vs. NHE)} \tag{8}$$

Chemical equilibria:

$$HCOOH \rightleftharpoons HCOO^- + H^+ \quad pK_a = 3.75 \tag{9}$$

$$CO_2 + H_2O \rightleftharpoons HCO_3^- + H^+ \quad pK_a = 6.35 \tag{10}$$

$$HCO_3^- \rightleftharpoons CO_3^{2-} + H^+ \quad pK_a = 10.33 \tag{11}$$

$$H_2O \rightleftharpoons OH^- + H^+ \quad pK_a = 15.74 \tag{12}$$

CO_2 is applied in excess and, therefore, partaking in chemical reactions with OH^- to produce minor amounts of HCO_3^- and CO_3^{2-}. Generated $HCOO^-$, OH^-, CO_3^{2-}, and HCO_3^- anions are transported through the anion exchange membrane to the center compartment, where they are protonated to form HCOOH, H_2O, and CO_2 after reaction with protons (reactions 9−12) stemming from the anode compartment.

■ DISCUSSION OF RESULTS

GDE Characterization. Spray-coating of Bi_2O_3 nanoparticle catalyst substrate, Vulcan conductive additive, and PiperION binder on carbon fiber substrate (TGP-H-120) achieved the custom-made GDE used in this work (Figure 2a, see Experimental Section for details). The same ionomer was employed both as a binder and for the AEM to ensure a good interface between the GDE and the AEM. Figure 2b depicts the scanning electron microscopy (SEM) image of the carbon fiber substrate before the catalyst coating. SEM magnifications on the prepared GDE (Figure 2c,d) present a fully covered carbon fiber substrate with a catalyst layer forming a coral-like surface structure. A more detailed distribution of the catalyst material can be seen at higher magnifications (Figure 2e,f). Herein, the catalyst nanoparticles, identified as bright agglomerates of spherical particles, display a rather homogeneous distribution on the surface.

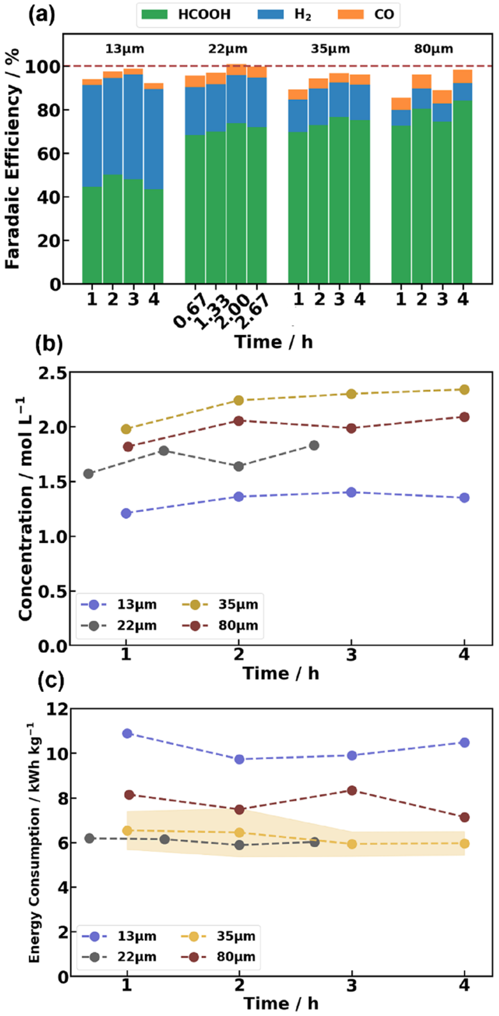

Figure 3. Key performance indicators (KPIs) of PiperION AEMs of various thicknesses vs experimental time: (a) Avg. faradaic efficiency (FE), (b) concentration of HCOOH (c_{FA}), and (c) specific energy consumption to HCOOH (Q_{FA}). Yellow background indicates experimental scatter for Q_{FA} (data shown in Figure S4). Constant current density was kept at 200 mA cm^{-2} and the center compartment flow rate at 100 μL min^{-1}.

General Flow Cell Characteristics. To ascertain the influence of the four PiperION AEMs of variable thicknesses (13, 22, 35, and 80 μm) on the performance of the three-compartment electrolyzer (Figures 3 and S3) measurements of the avg. cell voltage (U), avg. faradaic efficiencies (FEs), HCOOH concentration (c_{FA}), energy consumption to HCOOH (Q_{FA}), and production rate (P_{FA}) were conducted. During the experiments, the CO_2 was maintained in excess (60 mL min^{-1}), the current density was kept constant at 200 mA cm^{-2}, and the center compartment flow rate was set at 100 μL min^{-1} for 4 h. Membranes with thicknesses between 13 and 35 μm exhibited a nearly unchanged avg. cell voltage values during the measured experimental time (Figure S3a). The lowest cell voltage (3.7 V) was obtained using the 22 μm AEM, while voltages of 3.9 and 4.1 V were observed for the 35 and the 13 μm AEMs, respectively. However, the 80 μm membrane showed a significantly higher cell voltage of 5.0 V. The experimental scatter, calculated from three independent measurements using the 35 μm membrane, is in the range of 10−15% (yellow background in Figure S3a; calculations in Figure S4a), indicating a lack of correlation between the measured cell voltage and the membrane thickness. However, the thickest membrane does not follow this trend, which could be ascribed to lower levels of hydration under the tested conditions. Dehydration of the PiperION membrane would have an impact on the hydrophilic channel size and distribution, constraining the diffusion processes through the membrane, which results in higher resistance. Observed data variations are likely to be caused by the alteration of the internal resistance during the mechanical assembly process.

Table 1. Comparative Table Showcasing Key Performance Parameters Obtained in This Work and in the Literature

reference	this work	[18]	[45]	[46]
electrolyzer type	three-compartment electrolyzer	three-compartment electrolyzer	two-compartment electrolyzer	two-compartment (MEA) electrolyzer
ion-exchange membrane	PiperION (35 μm) – AEM	Sustainion X37-50 grade RT - AEM	Nafion 117 - CEM	Nafion 117 - CEM
catalyst	Bi_2O_3	Bi_2O_3	Bi/C	Bi/C
current density, mA cm^{-2}	200	200	200	100
cell voltage, V	3.9	3.5	4.2	3.1
faradaic efficiency ($HCOOH/HCOO^-$)	76%	76%	80%	41%
concentration ($HCOOH/HCOO^-$), mol L^{-1}	2.3	2.7	0.086	5.6
center compartment flow rate, μL min^{-1}	100	65	-	-
production rate ($HCOOH/HCOO^-$), mmol m^{-2} s^{-1}	7.9	7.8	8.3	2.1
specific energy consumption ($HCOOH/HCOO^-$), kWh kg^{-1}	5.9	5.4	6.0	8.9

Especially influenced is the center compartment due to the packing of the ion-exchange resin and the interface between the cathode and the AEM, which is influenced by the custom-made GDE preparation.[18,30] The measurement of the average faradaic efficiencies, as shown in Figure 3a, reveals an increase in the faradaic efficiency toward HCOOH (FE_{FA}) with thicker membranes. The highest FE_{FA} is achieved for the 80 μm (84%), followed by the 35 μm (76%), 22 μm (73%), and 13 μm AEM (50%). FE_{CO} also experiences a slight increase with a higher membrane thickness, albeit at a relatively low level (from 2 to 6% for the 13 and 80 μm AEM, respectively). In contrast, FE_{H2} decreases for an increasing membrane thickness (from ∼48 to 8% for the 13 and 80 μm AEMs, respectively). Thus, as membrane thickness increases, the selectivity of the CO_2 reduction reaction (CO_2RR) highly improves, which leads to HCOOH and a small amount of CO. The greatest change is observed when changing from 13 to 22 μm membrane, where the CO_2RR selectivity increases significantly from ∼50 to ∼73%. An important key performance indicator (KPI) for practical applications is the measurement of the concentration of HCOOH (c_{FA}) throughout the experimental time. This is maintained relatively constant for all four membranes, only subject to a marginal rise during the first 2 h (Figure 3b) and increases in value with the membrane thickness. Thus, the highest c_{FA} is obtained for the 35 μm (2.3 mol L^{-1}), followed by the 80 μm (2.0 mol L^{-1}), 22 μm (∼1.7 mol L^{-1}), and 13 μm membrane (∼1.3 mol L^{-1}). The comparatively low c_{FA} obtained for the thinner AEM agrees with its reduced FE_{FA}, since lower selectivity leads to the production of less HCOOH at a constant current density and water flow rate in the center compartment. An even more important KPI to be considered for industrial applications is the energy consumption, which is measured as kWh per kilo of HCOOH (Figure 3c). The representation of energy consumption over time displays a rather constant trend. The lowest and, therefore, best values are observed using the 22 and 35 μm membranes with ∼5.9 kWh kg^{-1} of HCOOH. The 80 μm AEM provided 8 kWh kg^{-1} of HCOOH due to the higher cell voltage. The highest energy consumption is obtained using the 13 μm membrane (10−11 kWh kg^{-1}) given the comparatively low selectivity toward HCOOH. Considering the amount of HCOOH obtained under the applied experimental conditions, that is, 200 mA cm^{-2} and 5 cm^2 of electrode area, Figure S3b provides valuable information regarding the production rate of HCOOH (P_{FA}). P_{FA} is constant during the 4 h of the experimental time for all four membranes. The 22, 35, and 80 μm membranes exhibit comparable P_{FA} values, appearing in the 7−8 mmol m^{-2} s^{-1} range, considering the experimental scattering, which is indicated by the yellow background. In contrast, the 13 μm AEM remains in the range of 4−5 mmol m^{-2} s^{-1}. This pronounced difference becomes evident when examining the lower FE_{FA} of the 13 μm AEM (Figure 3a) in contrast to its thicker analogues.[18]

When comparing these findings to the existing literature in the context of the same electrolyzer, the present results underline the viability of PiperION membranes as a valid alternative to Sustainion since PiperION leads to comparable results, particularly for the 35 μm AEM thickness (Table 1). At 200 mA cm^{-2}, a cell voltage of 3.9 V is achieved with PiperION, while 3.5 V is obtained with Sustainion. FEs_{FA} is approximately 76% in both cases.[18] Furthermore, using PiperION, a c_{FA} of 2.3 mol L^{-1} is obtained at a flow rate of 100 μL min^{-1} in the center compartment, while Sustainion provides 2.7 mol L^{-1} at a flow rate of 65 μL min^{-1}. In contrast, a slightly higher production rate to HCOOH is obtained using PiperION with 7.9 mmol m^{-2} s^{-1}, compared to 7.8 mmol m^{-2} s^{-1} for Sustainion. The result of Q_{FA} = 5.9 kWh kg^{-1} achieved in this work with PiperION is close to the lowest value for Sustainion reported in the literature to date (5.4 kWh kg^{-1}). The minor variations in cell performances observed between these two membranes can be attributed to fluctuations in the water flow rate, which has the potential to influence the concentration of produced HCOOH.[2]

Regarding the two-compartment electrolyzers, specifically membrane electrode assembly (MEA) electrolyzers, some advantages and disadvantages as in Table 1 become apparent. Three-compartment systems employ AEMs at the cathode, whereas two-compartment electrolyzers employ cation exchange membranes (CEMs). Utilizing bismuth-based catalysts at a current density of 200 mA cm^{-2}, these systems can achieve high faradaic efficiencies of up to 80% for formate production. However, the relatively high cell voltages and very low concentrations of formate (0.086 mol L^{-1}) result in specific energy consumptions of approximately 6.0 kWh kg^{-1} of formate. By contrast, employing a catholyte-free MEA electrolyzer significantly increases the concentration of formate to around 5.6 mol L^{-1}. Nevertheless, this process yields formate, which must be converted into formic acid through an energy-intensive process. Moreover, the current density is restricted to low values because increasing current density significantly decreases faradaic efficiency. The lowest overall

https://doi.org/10.1021/acs.iecr.3c04459
Ind. Eng. Chem. Res. 2024, 63, 3986−3996

energy consumption, with moderate concentrations of actual formic acid, is achieved using the three-compartment electrolyzer. This system offers a balanced approach, mitigating some of the limitations observed in two-compartment and catholyte-free MEA electrolyzers, making it a compelling option for efficient formic acid production.

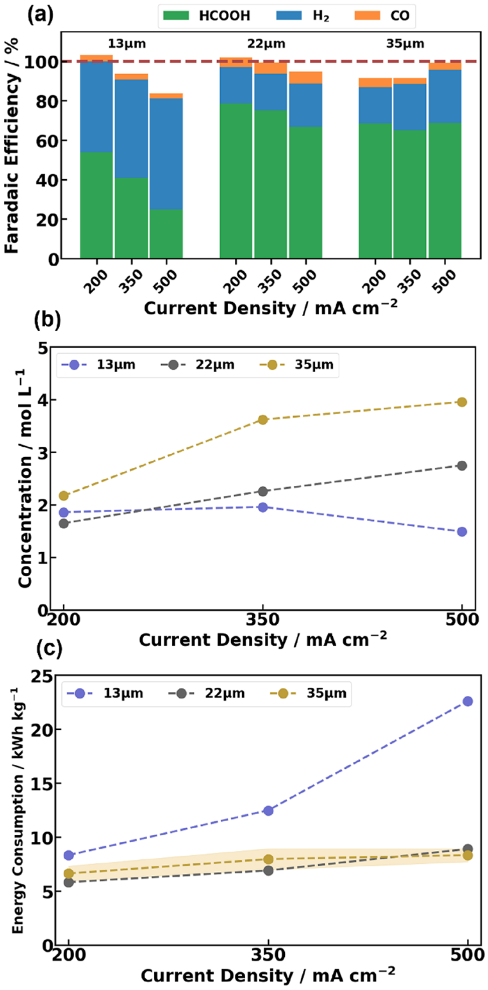

Figure 4. Key performance indicators (KPIs) of PiperION AEMs of various thicknesses vs current densities (j): (a) Avg. faradaic efficiency (FE), (b) concentration of HCOOH (c_{FA}), and (c) specific energy consumption to HCOOH (Q_{FA}). Yellow background indicates experimental scatter for Q_{FA} (data shown in Figure S4). Center compartment flow rate was kept at 100 μL min^{-1}. Current densities were maintained for 1 h.

Impact of Current Density. Considering the prior information, the assessment of the cell's performance under different current densities (200, 350, and 500 mA cm^{-2}) was conducted for the three AEMs with thicknesses of 13, 22, and 35 μm. CO_2 was maintained in excess, and the center compartment flow rate was kept at 100 μL min^{-1}. The avg. cell voltage at various current densities revealed a consistent rise of the cell voltage from 4.0 to ~5.0 V (Figure S5a) for AEM thicknesses of 13 to 35 μm. The thickest membrane (80 μm) could not be measured at current densities of 350 and 500 mA cm^{-2}. Even at 150 and 250 mA cm^{-2}, cell voltages reach values as high as 5.0 and 5.6 V, respectively (Figure S5). As previously mentioned, local dehydration of the AEM during operation at increased current densities would significantly increase the resistance. Further investigations in this regard were not conducted as they deviated from the main topic. FE_{FA} improved with increasing membrane thicknesses from 13 to 22 μm and showed slightly lower values for the 35 μm membrane for each investigated current density (Figure 4a). However, within the same membrane thickness, the increase of current density led to a decrease of FE_{FA}, which was negligible for the 35 μm membrane. FE_{FA} of 65−78% was observed for the 22 and 35 μm AEMs, while lower FEs_{FA} was achieved for the 13 μm membrane (53% at 200 mA cm^{-2} and 25% at 500 mA cm^{-2}). The increase of selectivity toward HCOOH for increasing membrane thickness from 13 to 22 μm is also correlated with increasing FE_{CO}, demonstrating an enhancement of the overall CO_2 electroreduction. Nonetheless, the CO evolution is comparatively low, 3−6% for all investigated current densities and AEM thicknesses. In contrast, FE_{H_2} declines with thicker membranes while demonstrating modest increments with higher current densities. The lowest FE_{H_2} values are observed at 200 mA cm^{-2} using the 22 and 35 μm membranes (18%), while the highest value (56%) is obtained with the 13 μm membrane at 500 mA cm^{-2}. The employment of high current densities results in higher c_{FA} values when using the 22 and 35 μm membranes, which can be attributed to a greater production rate at an unchanged flow rate of water to the center compartment. However, the thinnest membrane exhibits a minimum at 500 mA cm^{-2}. The highest c_{FA} of ~4.0 mol L^{-1} is obtained using the 35 μm membrane, followed by the 22 μm membrane with 2.8 mol L^{-1}, both at 500 mA cm^{-2}. In contrast, the 13 μm membrane allows for the highest c_{FA} at 350 mA cm^{-2} with 2.0 mol L^{-1}, which decreases to 1.5 mol L^{-1} at 500 mA cm^{-2}. At higher current densities, energy consumption to produce HCOOH (Q_{FA}) displays a slight increase when employing AEMs of 22 and 35 μm. In contrast, at 500 mA cm^{-2}, a sharp increase is obtained with the 13 μm membrane (Figure 4c). Thus, Q_{FA} ranges from 5.9 to 8.9 kWh kg^{-1} with the 22 and 35 μm membranes, which is achieved with current densities spanning from 200 to 500 mA cm^{-2}. However, using the 13 μm AEM, Q_{FA} increases to 22.6 kWh kg^{-1} at 500 mA cm^{-2}, due to the low FE_{FA} at this current density. Production rates increase with rising current density (Figure S5b) allowing maximum values of 17.3 and 17.8 mmol m^{-2} s^{-1} at 500 mA cm^{-2}, with 22 and 35 μm PiperION AEMs, respectively. These values correspond to ~67% of the theoretical maximum as indicated by the solid red line in Figure S5b. The thickest membrane follows this trend, exhibiting a comparable slope, albeit only reaching the P_{FA} value of 9.2 mmol m^{-2} s^{-1} at the maximum applicable current density of 250 mA cm^{-2}. However, the thinnest membrane does not follow this behavior, maintaining a rather stable P_{FA} value of ~6 mmol m^{-2} s^{-1} at the studied current densities.

These experiments provide valuable insights, particularly considering the significance of maintaining alkaline conditions around the Bi_2O_3-based GDE for achieving optimal catalytic efficiency and selective HCOOH production. At the lowest current density, the influence of the center compartment acidity on the alkaline cathodic environment is relatively low for the 22 and 35 μm PiperION AEMs, as indicated by their low FE_{H2} and high c_{FA} (Figure 4a,b). However, the smaller separation provided by the 13 μm membrane results in a reduction in the pH value around the cathodic GDE, resulting in lower FE_{FA} and increased FE_{H2}. At 500 mA cm^{-2}, a higher c_{FA} can be anticipated due to the increased electron density, which fosters electrochemical CO_2 conversion to $HCOO^-$ and accelerates transport phenomena. Therefore, 22 and 35 μm membranes serve as a protective barrier shielding the cathodic compartment from the acidic center, resulting in high FE_{FA} and c_{FA} values (Figure 4a,b). On the contrary, the 13 μm membrane fails to maintain the necessary operating conditions in the cathode, resulting in a decline of FE_{FA} and promoting the hydrogen evolution reaction (Figure 4a).

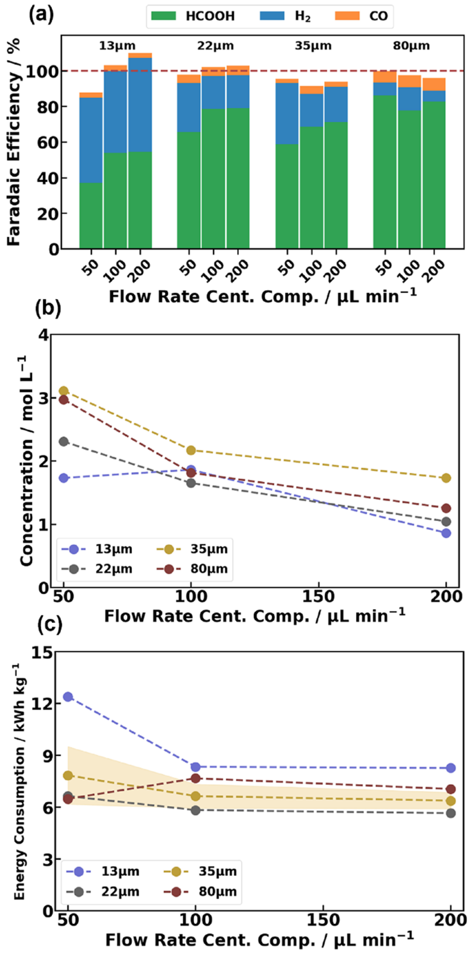

Figure 5. Key performance indicators (KPIs) of PiperION AEMs of various thicknesses vs flow rate in the center compartment: (a) Avg. faradaic efficiency (FE), (b) concentration of HCOOH (c_{FA}), and (c) specific energy consumption to HCOOH (Q_{FA}). Yellow background indicates experimental scatter for Q_{FA} (data shown in Figure S4). Current density was kept constant at 200 mA cm^{-2}.

Impact of Center Compartment Flow Rate. To assess the influence of the center compartment flow rate on the performance of the electrolytic process, a series of experiments (Figures 5 and S6) were conducted by using the four investigated AEMs, all operating at 200 mA cm^{-2}. The center compartment flow rates studied were 50, 100, and 200 μL min^{-1}. These flow rates do not exert any significant influence on the cell voltage, which remains constant in the range of 3.9−4.0 V for the 13, 22, and 35 μm and ∼5.0 V for the 80 μm AEM (Figure S6, left). However, they inflict major changes in the FE (Figure 5a). The increase in the flow rate entails higher FEs_{FA} and FEs_{CO} for the 13, 22, and 35 μm AEMs. FE_{H2} exhibits an inverse trend with lower efficiencies obtained for higher flow rates. However, the 80 μm AEM provides the highest FE_{FA} at 50 μL min^{-1} with 86%. AEMs with thicknesses of 13, 22, and 35 μm achieve FEs_{FA} of 55, 79, and 71%, respectively, at a flow rate of 200 μL min^{-1}. FEs_{CO} in the studied membranes and flow rates are in the range 3−7%. FE_{H2} reaches a peak of ∼49% with the 13 μm membrane but experiences a significant decline as the membrane thickness increases. The impact of the center compartment flow rate on the concentration of HCOOH (c_{FA}) is depicted in Figure 5b. High c_{FA} values are achieved at 50 μL min^{-1} for the four membranes (3.1, 3.0, 2.3, and 1.7 mol L^{-1} for the 35, 80, 22, and 13 μm AEMs, respectively), decreasing with increasing flow rates. This can be explained by the fact that an increase in the flow rate results in a greater dilution of HCOOH. An evaluation of the energy consumption for HCOOH production (Q_{FA}) reveals that the 22, 35, and 80 μm AEMs exhibit an energy efficiency with 6.6, 7.8, and 6.5 kWh kg^{-1} of HCOOH at 50 μL min^{-1}, respectively (Figure 5c). While at 100 and 200 μL min^{-1}, the 22 and 35 μm membranes display slightly lower Q_{FA} values, and the 13 μm membrane shows a more pronounced decline. Hence, a reduction in the center compartment flow rate leads to an increase in Q_{FA}, with this effect being more accentuated for the 13 μm membrane. Due to the dilution effect observed at high flow rates, c_{FA} and Q_{FA} are deemed as less representative indicators, favoring FE_{FA} as more reliable. The improvement in FE_{FA} with increased flow rates could be linked to the dilution effect, which lowers the local pH value in the central compartment, subsequently enhancing the catalyst's efficiency at the cathode. Figure S6 (right) shows an P_{FA} constant between 100 and 200 μL min^{-1} for all membranes. At 50 μL min^{-1}, 13, 22, and 35 μm AEMs present a significant decrease in the production rate. However, with the 80 μm membrane, the P_{FA} value rises to a maximum of 9 mmol m^{-2} s^{-1}, highlighting its high selectivity toward HCOOH at the lowest flow rate.

Influence of Initial HCOOH Concentration on Faradaic Efficiency. To conduct a more in-depth analysis of the impact of acidity in the studied electrolyzer, various c_{FA}s (0, 0.924, 2.391, and 4.201 mol L^{-1}) were explored to be used as an electrolyte in the center compartment with current densities in the range of 200−500 mA cm^{-2}. To achieve a homogeneous and rather approximately constant c_{FA} over the measurement time, a higher flow as previously applied was used during these experiments (3 mL min^{-1}). With this the vertically upward concentration gradient in the center compartment is diminished as the formic acid concentration at in- and outlet is nearly equal. The time for each experiment was set to 0.5 h. FE_{H2} rises as c_{FA} increases, and the applied current density decreases, showing the highest FE_{H2} (44%) at j = 200 mA cm^{-2} and c_{FA} = 4.201 mol L^{-1} (Figure 6a). The lowest FEs_{H2} are achieved at 500 mA cm^{-2}, where values ramp up from 11 to 31% as c_{FA} increases. Values of FE_{CO} follow the opposite trend, and they increase as c_{FA} decreases and the applied current density increases (Figure 6b). The highest FE_{CO} values occur at 500 mA cm^{-2} with 6.4% (c_{FA} = 0) and 4.9% (c_{FA} = 4.201 mol L^{-1}). Calculating FEs_{FA} from the analyzed c_{FA} data would introduce significant uncertainty, given the minimal amount of HCOOH produced compared to the initial concentration (Figure S7). Consequently, considering that the only observed products (by GC and IC) are HCOOH, CO, and H_2, FE_{FA} is calculated as the remaining FE from prior calculations of FE_{CO} and FE_{H2}. FE_{FA} exhibits a trend similar to that of FE_{CO} (FE_{FA} increases as c_{FA} decreases and the applied current density increases) (Figure 6c). The highest efficiencies are obtained at 500 mA cm^{-2} with values ranging from 82%

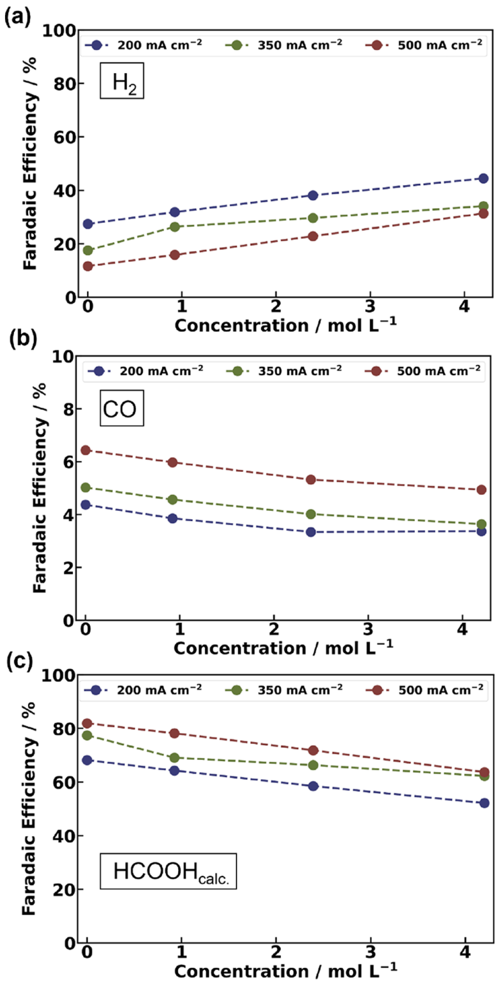

Figure 6. Faradaic efficiency (FE) vs various HCOOH concentrations (c_{FA}) (0, 0.924, 2.391, and 4.201 mol L^{-1}): (a) FE_{H2} vs c_{FA}, (b) FE_{CO} vs c_{FA}, and (c) FE_{FA} vs c_{FA}. Current densities are in the range 200–500 mA cm^{-2}, the experimental time is 0.5 h, and the center compartment flow rate is 3 mL min^{-1}.

(c_{FA} = 0) to 64% (c_{FA} = 4.201 mol L^{-1}). Lower current intensities resulted in a lower FE_{FA}.

These results indicate that higher c_{FA} in the center compartment promotes back diffusion of HCOOH toward the cathode, shifting the local reaction environment to a lower pH value, as previously observed by other authors,[18,47] affecting the values of FE_{FA} negatively. Furthermore, at a constant c_{FA} in the center compartment, a higher current density results in greater alkalinity at the cathode, attributed to the increase of OH^- ions during the CO_2 electroreduction. These later experiments virtually shift the formic acid concentration gradient across the AEM for one AEM of a given thickness. Consequently, they reinforce the concept that thicker membranes act as effective barriers, shielding the cathode from the acidic pH of the center compartment. This, in turn, enhances the efficiency of the CO_2 electroreduction process.

.

Final Remarks. The impact of utilizing different PiperION AEM thicknesses on the CO_2 electroreduction performance (to HCOOH) has been discussed under the application of different operating conditions, that is, experimental time (Figure 3), current density (Figure 4), and center compartment flow rate (Figure 5). These results clearly illustrate that the thickness of the PiperION AEM has a significant effect on the key performance indicators (KPIs) examined here. In general, the PiperION membranes with a thickness of 22 and 35 μm lead to superior performances, including high faradaic efficiency (FE_{FA}), concentration (c_{FA}), and relatively low energy consumption for the generation of HCOOH (Q_{FA}). Conversely, the thinnest membrane (13 μm) provided a low FE_{FA}, resulting in comparatively low c_{FA} and high Q_{FA}. The thickest investigated membrane (80 μm) introduced a higher inner resistance into the electrolyzer, resulting in significantly higher cell voltages, which, in contrast to the medium-thick membranes, could not be compensated with higher FE_{FA}. The presence of the strongly acidic ion-exchange resin, utilized to facilitate the transfer of protons from the anode, along with the generated HCOOH, results in an acidic pH within the central

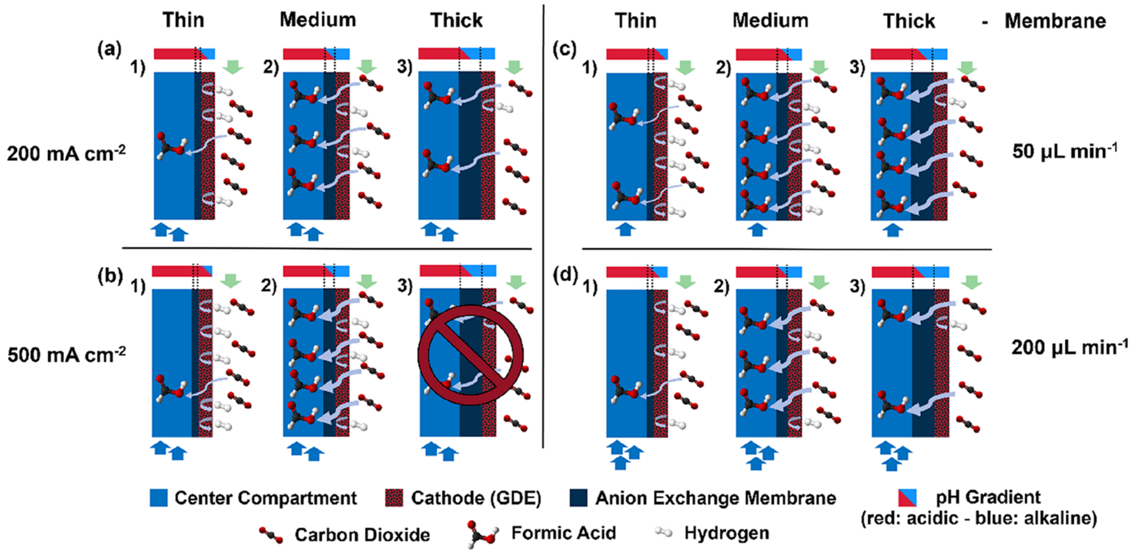

Figure 7. Illustration of the cathodic local reaction environment using thin (13 μm), medium (22 or 35 μm), and thick (80 μm) PiperION AEMs under different operating parameters. Current densities: (a) 200 mA cm^{-2} and (b) 500 mA cm^{-2}. Center compartment flow rates under a constant current density of 200 mA cm^{-2}: (c) 50 μL min^{-1} and (d) 200 μL min^{-1}.

compartment. Nevertheless, it is important to note that the reaction environment in the gas diffusion electrode (GDE) when employing Bi-based catalysts is alkaline[30,36] and their catalytic efficiency and selectivity, which are optimal in alkaline media, are notably affected by variations in pH levels at the cathode.[5,18,48−50] Hence, the AEM serves as a barrier separating the acidic center compartment from the alkaline cathodic environment, leading to the formation of a pH gradient. One influencing parameter is the back diffusion of HCOOH and water from the center compartment to the cathode. Especially, the back diffusion of HCOOH decreases the local pH value at the cathode. This, however, can be reduced by implementing thicker membranes. The thickness of the membrane proves to be a critical factor in determining the performance of the electrolyzer, as investigated in this study. A visual depiction of the described processes is presented in Figures 7 and S9 and explained in detail in the Supporting Information. The most important information from the illustration is that the PiperION thin membrane is unsuitable for a three-compartment electrolyzer since the barrier function between the acidic center compartment and the alkaline reaction environment at the cathode GDE is low. Only a comparatively high flow rate (Figure 7d (1)) would allow for application, but at low HCOOH concentrations. On the other hand, the thick PiperION AEM provides an effective barrier, albeit adding a higher inner resistance to the cell, which causes high cell voltages. Besides, although high concentrations of HCOOH are achievable (Figure 7a,c (3)), they come at a high energy consumption. The most suitable membranes for the three-compartment electrolyzer are medium-thick (22 or 35 μm) given their low specific energy consumption and comparatively high resulting concentrations of HCOOH (Figure 7a−d, (2)).

CONCLUSIONS

In summary, PiperION AEMs of different thicknesses revealed a significant effect on the efficiency of the applied three-compartment electrolyzer. At 200 mA cm^{-2}, 22 and 35 μm membranes presented the best overall performances resulting in average cell voltages in the range of 3.7−3.9 V, faradaic efficiencies of 73−76%, and an average energy consumption for the generation of HCOOH of ~5.9 kWh kg^{-1}. The observed faradaic efficiencies and specific energy consumptions for HCOOH are comparable to the results obtained for Sustainion AEMs in a similar setup, making PiperION AEMs viable alternatives in the context of direct CO_2 electroreduction to HCOOH. Furthermore, this study demonstrates that the appropriate thickness of these membranes is critical to establishing a pH gradient between the center and cathodic compartment to favor an alkaline environment around the catalyst. This condition was obtained with the medium and thick AEMs, which were capable of shielding the alkaline environment in the GDE from the acidic center compartment. In contrast, thin membranes such as the 13 μm PiperION prove unsuitable under the reported conditions, evident from their low faradaic efficiencies and high specific energy consumptions.

ASSOCIATED CONTENT

Supporting Information

The Supporting Information is available free of charge at https://pubs.acs.org/doi/10.1021/acs.iecr.3c04459.

A photo of the experimental setup used in the laboratory (Figure S1); pictures of the electrolyzer components (Figure S2), cell voltage and production rate of HCOOH vs experimental time (Figure S3); scattering of the cell voltage, energy consumption of HCOOH, and faradaic efficiencies of three independent measurements using the 35 μm PiperION membrane (Figure S4); cell voltage, production rate of HCOOH, concentration, energy consumption, and faradaic efficiency vs current density (Figure S5); cell voltage and production rate of HCOOH vs flow rate in the center compartment (Figure S6), and the resulting HCOOH concentrations using various starting concentrations of HCOOH during CO_2 electroreduction at various current densities (Figure S7); illustration of the cathodic local reaction environment and detailed description (Figure S8); simplified illustration of the cathodic local reaction environment in a three-compartment electrolyzer for formic acid production (Figure S9) (PDF)

AUTHOR INFORMATION

Corresponding Author

Bastian Rutjens − *Institute of Energy and Climate Research − Fundamental Electrochemistry (IEK-9), Forschungszentrum Jülich GmbH, 52428 Jülich, Germany; Institute of Physical Chemistry, RWTH Aachen University, 52074 Aachen, Germany*; orcid.org/0000-0002-7411-6511; Email: b.rutjens@fz-juelich.de

Authors

Konstantin von Foerster − *Institute of Energy and Climate Research − Fundamental Electrochemistry (IEK-9), Forschungszentrum Jülich GmbH, 52428 Jülich, Germany; Institute of Physical Chemistry, RWTH Aachen University, 52074 Aachen, Germany*

Bernhard Schmid − *Institute of Energy and Climate Research − Fundamental Electrochemistry (IEK-9), Forschungszentrum Jülich GmbH, 52428 Jülich, Germany*

Henning Weinrich − *Institute of Energy and Climate Research − Fundamental Electrochemistry (IEK-9), Forschungszentrum Jülich GmbH, 52428 Jülich, Germany*; orcid.org/0000-0001-9946-6078

Sergio Sanz − *Institute of Energy and Climate Research − Fundamental Electrochemistry (IEK-9), Forschungszentrum Jülich GmbH, 52428 Jülich, Germany*

Hermann Tempel − *Institute of Energy and Climate Research − Fundamental Electrochemistry (IEK-9), Forschungszentrum Jülich GmbH, 52428 Jülich, Germany*; orcid.org/0000-0002-9794-6403

Rüdiger-A. Eichel − *Institute of Energy and Climate Research − Fundamental Electrochemistry (IEK-9), Forschungszentrum Jülich GmbH, 52428 Jülich, Germany; Institute of Physical Chemistry, RWTH Aachen University, 52074 Aachen, Germany*; orcid.org/0000-0002-0013-6325

Complete contact information is available at:
https://pubs.acs.org/10.1021/acs.iecr.3c04459

Author Contributions

B.R., H.W., and R.-A.E. conceived the idea. B.R. and K.v.F. collected the data. B.R., K.v.F., H.W., and B.S. analyzed and interpreted the data. All authors contributed to the writing and editing of the manuscript.

Funding

Federal Ministry of Education and Research (BMBF). Project: iNEW2.0 'iNEW2.0 − Inkubator Nachhaltige Elektrochemische Wertschöpfungsketten' (Funding code: 03SF0627A)

Notes

The authors declare no competing financial interest.

■ ACKNOWLEDGMENTS

The authors kindly acknowledge the financial support from the German Federal Ministry of Education and Research (BMBF) within the project 'iNEW2.0 − Inkubator Nachhaltige Elektrochemische Wertschöpfungsketten' Project No. 03SF0627A.

■ ABBREVIATIONS

DFAFCs, direct formic acid fuel cells; CEM, cation exchange membrane; AEM, anion exchange membrane; GDE, gas diffusion electrode; IC, ion chromatography; GC, gas chromatography; OCP, open circuit potential; PEIS, potentiostatic electrochemical impedance spectroscopy; LSV, linear sweep voltammetry; CA, chronoamperometry; CP, chronopotentiometry; KPI, key performance indicator; FE, faradaic efficiency; FA, formic acid; HER, hydrogen evolution reaction; MEA, membrane electrode assembly

■ REFERENCES

(1) Zimmermann, A. W.; Langhorst, T.; Moni, S.; Schaidle, J. A.; Bensebaa, F.; Bardow, A. Life-Cycle and Techno-Economic Assessment of Early-Stage Carbon Capture and Utilization Technologies—A Discussion of Current Challenges and Best Practices. *Frontiers in Climate* **2022**, *4* (March), 1−12.

(2) Ellabban, O.; Abu-Rub, H.; Blaabjerg, F. Renewable Energy Resources: Current Status, Future Prospects and Their Enabling Technology. *Renewable and Sustainable Energy Reviews* **2014**, *39*, 748−764.

(3) Sánchez, O. G.; Birdja, Y. Y.; Bulut, M.; Vaes, J.; Breugelmans, T.; Pant, D. Recent Advances in Industrial CO2 Electroreduction. *Curr. Opin Green Sustain Chem.* **2019**, *16*, 47−56.

(4) Birdja, Y. Y.; Pérez-Gallent, E.; Figueiredo, M. C.; Göttle, A. J.; Calle-Vallejo, F.; Koper, M. T. M. Advances and Challenges in Understanding the Electrocatalytic Conversion of Carbon Dioxide to Fuels. *Nat. Energy* **2019**, *4* (9), 732−745.

(5) Hori, Y. Electrochemical CO2 Reduction on Metal Electrodes. In *Modern Aspects of Electrochemistry*; Springer: New York: New York, NY, 2008; pp 89−189. DOI: 10.1007/978-0-387-49489-0_3.

(6) Quentmeier, M.; Schmid, B.; Tempel, H.; Kungl, H.; Eichel, R.-A. Toward a Stackable CO_2-to-CO Electrolyzer Cell Design—Impact of Media Flow Optimization. *ACS Sustain Chem. Eng.* **2023**, *11* (2), 679−688.

(7) Jin, S.; Hao, Z.; Zhang, K.; Yan, Z.; Chen, J. Advances and Challenges for the Electrochemical Reduction of CO_2 to CO: From Fundamentals to Industrialization. *Angew. Chem., Int. Ed.* **2021**, *60* (38), 20627−20648.

(8) Jeanty, P.; Scherer, C.; Magori, E.; Wiesner-Fleischer, K.; Hinrichsen, O.; Fleischer, M. Upscaling and Continuous Operation of Electrochemical CO2 to CO Conversion in Aqueous Solutions on Silver Gas Diffusion Electrodes. *J. CO2 Util.* **2018**, *24* (January), 454−462.

(9) Vennekoetter, J.-B.; Sengpiel, R.; Wessling, M. Beyond the Catalyst: How Electrode and Reactor Design Determine the Product Spectrum during Electrochemical CO2 Reduction. *Chemical Engineering Journal* **2019**, *364*, 89−101.

(10) Reinisch, D.; Schmid, B.; Martić, N.; Krause, R.; Landes, H.; Hanebuth, M.; Mayrhofer, K. J. J.; Schmid, G. Various CO_2-to-CO Electrolyzer Cell and Operation Mode Designs to Avoid CO_2-Crossover from Cathode to Anode. *Zeitschrift für Physikalische Chemie* **2020**, *234* (6), 1115−1131.

(11) Reichbauer, T.; Schmid, B.; Vetter, K.; Reinisch, D.; Martić, N.; Reller, C.; Grasruck, A.; Dorta, R.; Schmid, G. Electrical Energy Input Efficiency Limitations in CO_2-to-CO Electrolysis and Attempts for Improvement. *Electrochemical Science Advances* **2023**, *August*, 1−16.

(12) Zhang, T.; Bui, J. C.; Li, Z.; Bell, A. T.; Weber, A. Z.; Wu, J. Highly Selective and Productive Reduction of Carbon Dioxide to Multicarbon Products via in Situ CO Management Using Segmented Tandem Electrodes. *Nat. Catal* **2022**, *5* (3), 202−211.

(13) Larrazábal, G. O.; Okatenko, V.; Chorkendorff, I.; Buonsanti, R.; Seger, B. Investigation of Ethylene and Propylene Production from CO_2 Reduction over Copper Nanocubes in an MEA-Type Electrolyzer. *ACS Appl. Mater. Interfaces* **2022**, *14* (6), 7779−7787.

(14) Gao, D.; Arán-Ais, R. M.; Jeon, H. S.; Roldan Cuenya, B. Rational Catalyst and Electrolyte Design for CO2 Electroreduction towards Multicarbon Products. *Nat. Catal* **2019**, *2* (3), 198−210.

(15) Hecker, B.; Robens, E.; Valencia, H. E.; Windmüller, A.; Muench, F.; Meledina, M.; Tempel, H.; Kungl, H.; Mayer, J.; Eichel, R.-A. Effects of Synthesized Silver Nanoplate Structures on the Electrochemical Reduction of CO_2. *J. Electrochem. Soc.* **2023**, *170* (9), No. 096505.

(16) Robens, E.; Hecker, B.; Kungl, H.; Tempel, H.; Eichel, R.-A. Bimetallic Copper−Silver Catalysts for the Electrochemical Reduction of CO_2 to Ethanol. *ACS Appl. Energy Mater.* **2023**, *6* (14), 7571−7577.

(17) Weinrich, H.; Rutjens, B.; Basak, S.; Schmid, B.; Camara, O.; Kretzschmar, A.; Kungl, H.; Tempel, H.; Eichel, R.-A. CO2 Electroreduction to Formate-Comparative Study Regarding the Electrocatalytic Performance of SnO 2 Nanoparticles. *catalysts* **2023**, *13* (5), 903.

(18) Yang, H.; Kaczur, J. J.; Sajjad, S. D.; Masel, R. I. Performance and Long-Term Stability of CO2 Conversion to Formic Acid Using a Three-Compartment Electrolyzer Design. *J. CO2 Util.* **2020**, *42* (October), No. 101349.

(19) Ikemiya, N.; Natsui, K.; Nakata, K.; Einaga, Y. Long-Term Continuous Conversion of CO_2 to Formic Acid Using Boron-Doped Diamond Electrodes. *ACS Sustain Chem. Eng.* **2018**, *6* (7), 8108−8112.

(20) Fernández-Caso, K.; Díaz-Sainz, G.; Alvarez-Guerra, M.; Irabien, A. Electroreduction of CO_2: Advances in the Continuous Production of Formic Acid and Formate. *ACS Energy Lett.* **2023**, *8* (4), 1992−2024.

(21) Theußl, V.; Weinrich, H.; Heume, C.; Dzieciol, K.; Schmid, B.; Kungl, H.; Tempel, H.; Eichel, R. Impact of the Carbon Substrate for Gas Diffusion Electrodes on the Electroreduction of CO_2 to Formate. *ChemElectroChem.* **2023**, *10* (17), No. e202300121.

(22) Baessler, J.; Oliveira, T.; Keller, R.; Wessling, M. Paired Electrosynthesis of Formic Acid from CO_2 and Formaldehyde from Methanol. *ACS Sustain Chem. Eng.* **2023**, *11* (18), 6822−6828.

(23) Vehrenberg, J.; Baessler, J.; Decker, A.; Keller, R.; Wessling, M. Paired Electrochemical Synthesis of Formate via Oxidation of Glycerol and Reduction of CO2 in a Flow Cell Reactor. *Electrochem commun* **2023**, *151*, No. 107497.

(24) Chanda, D.; Lee, S.; Tufa, R. A.; Kim, Y. J.; Xing, R.; Meshesha, M. M.; Demissie, T. B.; Liu, S.; Pant, D.; Santoro, S.; Kim, K.; Yang, B. L. Gas-Phase CO2 Electrolysis Using Carbon-Derived Bismuth Nanospheres on Porous Nickel Foam Gas Diffusion Electrode. *Int. J. Hydrogen Energy* **2024**, *56*, 1020−1031.

(25) Aslam, N. M.; Masdar, M. S.; Kamarudin, S. K.; Daud, W. R. W. Overview on Direct Formic Acid Fuel Cells (DFAFCs) as an Energy Sources. *APCBEE Procedia* **2012**, *3*, 33−39.

(26) Eppinger, J.; Huang, K. W. Formic Acid as a Hydrogen Energy Carrier. *ACS Energy Letters.*; American Chemical Society January 13, 2017; pp 188−195. DOI: 10.1021/acsenergylett.6b00574.

(27) Spurgeon, J. M.; Kumar, B. A Comparative Technoeconomic Analysis of Pathways for Commercial Electrochemical CO_2 Reduction to Liquid Products. *Energy Environ. Sci.* **2018**, *11* (6), 1536−1551.

(28) Jordaan, S. M.; Wang, C. Electrocatalytic Conversion of Carbon Dioxide for the Paris Goals. *Nat. Catal* **2021**, *4* (11), 915−920.

(29) Bulushev, D. A.; Ross, J. R. H. Towards Sustainable Production of Formic Acid. *ChemSusChem* **2018**, *11* (5), 821−836.

(30) Yang, H.; Kaczur, J. J.; Sajjad, S. D.; Masel, R. I. Electrochemical Conversion of CO2 to Formic Acid Utilizing Sustainion^{TM} Membranes. *Journal of CO2 Utilization* **2017**, *20* (June), 208−217.

(31) Li, F.; Fan, Z.; Tai, J.; Wei, H.; Zhou, Y.; Lei, L. Promoting the Electrochemical Reduction of Carbon Dioxide by a Specially Designed Biomimetic Electrochemical Cell. *Ind. Eng. Chem. Res.* **2018**, *57* (37), 12307−12313.

(32) Xia, C.; Zhu, P.; Jiang, Q.; Pan, Y.; Liang, W.; Stavitski, E.; Alshareef, H. N.; Wang, H. Continuous Production of Pure Liquid Fuel Solutions via Electrocatalytic CO2 Reduction Using Solid-Electrolyte Devices. *Nat. Energy* **2019**, *4* (9), 776−785.

(33) Li, Z.; Zhang, T.; Yadav, R. M.; Zhang, J.; Wu, J. Boron Doping in Tin Catalysts Towards Gas-Phase CO_2 to Formic Acid/Formate Electroreduction with High Production Efficiency and Rate. *J. Electrochem. Soc.* **2020**, *167* (11), No. 114508.

(34) Zhu, P.; Wang, H. High-Purity and High-Concentration Liquid Fuels through CO2 Electroreduction. *Nat. Catal* **2021**, *4* (11), 943−951.

(35) Zheng, T.; Liu, C.; Guo, C.; Zhang, M.; Li, X.; Jiang, Q.; Xue, W.; Li, H.; Li, A.; Pao, C.-W.; Xiao, J.; Xia, C.; Zeng, J. Copper-Catalysed Exclusive CO2 to Pure Formic Acid Conversion via Single-Atom Alloying. *Nat. Nanotechnol* **2021**, *16* (12), 1386−1393.

(36) Radersma, W. Y. M.; Anastasopol, A.; Latsubaia, R.; Perez Gallent, E.; Gilling, E.; Goetheer, E. Modelling of Formic Acid in Situ Separation in a Three Compartment Electrolyzer. *SSRN Electronic Journal* **2019**, *October*, 1−16.

(37) Kaczur, J. J.; Yang, H.; Liu, Z.; Sajjad, S. D.; Masel, R. I. Carbon Dioxide and Water Electrolysis Using New Alkaline Stable Anion Membranes. *Front Chem.* **2018**, *6* (JUL), 1−16.

(38) Hu, X.; Huang, Y.; Liu, L.; Ju, Q.; Zhou, X.; Qiao, X.; Zheng, Z.; Li, N. Piperidinium Functionalized Aryl Ether-Free Polyaromatics as Anion Exchange Membrane for Water Electrolysers: Performance and Durability. *J. Membr. Sci.* **2021**, *621*, No. 118964.

(39) Luo, X.; Rojas-Carbonell, S.; Yan, Y.; Kusoglu, A. Structure-Transport Relationships of Poly(Aryl Piperidinium) Anion-Exchange Membranes: Eeffect of Anions and Hydration. *J. Membr. Sci.* **2020**, *598*, No. 117680.

(40) Du, X.; Zhang, H.; Yuan, Y.; Wang, Z. Constructing Micro-Phase Separation Structure to Improve the Performance of Anion-Exchange Membrane Based on Poly(Aryl Piperidinium) Cross-Linked Membranes. *J. Power Sources* **2021**, *487* (October 2020), No. 229429.

(41) Endrődi, B.; Kecsenovity, E.; Samu, A.; Halmágyi, T.; Rojas-Carbonell, S.; Wang, L.; Yan, Y.; Janáky, C. High Carbonate Ion Conductance of a Robust PiperION Membrane Allows Industrial Current Density and Conversion in a Zero-Gap Carbon Dioxide Electrolyzer Cell. *Energy Environ. Sci.* **2020**, *13* (11), 4098−4105.

(42) White, J. L.; Herb, J. T.; Kaczur, J. J.; Majsztrik, P. W.; Bocarsly, A. B. Photons to Formate: Efficient Electrochemical Solar Energy Conversion via Reduction of Carbon Dioxide. *Journal of CO2 Utilization* **2014**, *7*, 1−5.

(43) Zhang, W.; Hu, Y.; Ma, L.; Zhu, G.; Wang, Y.; Xue, X.; Chen, R.; Yang, S.; Jin, Z. Progress and Perspective of Electrocatalytic CO_2 Reduction for Renewable Carbonaceous Fuels and Chemicals. *Adv. Sci.* **2018**, *5* (1), No. 1700275.

(44) Riedel, E.; Meyer, H.-J. *Allgemeine Und Anorganische Chemie*, 11th ed.; De Gruyter, 2013; Vol. *11*.

(45) Díaz-Sainz, G.; Alvarez-Guerra, M.; Solla-Gullón, J.; García-Cruz, L.; Montiel, V.; Irabien, A. CO2 Electroreduction to Formate: Continuous Single-Pass Operation in a Filter-Press Reactor at High Current Densities Using Bi Gas Diffusion Electrodes. *Journal of CO2 Utilization* **2019**, *34* (March), 12−19.

(46) Díaz-Sainz, G.; Alvarez-Guerra, M.; Ávila-Bolívar, B.; Solla-Gullón, J.; Montiel, V.; Irabien, A. Improving Trade-Offs in the Figures of Merit of Gas-Phase Single-Pass Continuous CO2 Electrocatalytic Reduction to Formate. *Chem. Eng. J.* **2021**, *405* (September 2020), No. 126965.

(47) Hu, L.; Wrubel, J. A.; Baez-Cotto, C. M.; Intia, F.; Park, J. H.; Kropf, A. J.; Kariuki, N.; Huang, Z.; Farghaly, A.; Amichi, L.; Saha, P.; Tao, L.; Cullen, D. A.; Myers, D. J.; Ferrandon, M. S.; Neyerlin, K. C. A Scalable Membrane Electrode Assembly Architecture for Efficient Electrochemical Conversion of CO2 to Formic Acid. *Nat. Commun.* **2023**, *14* (1), 7605.

(48) Yu, Z.-L.; Wu, S.-Q.; Chen, L.-W.; Hao, Y.-C.; Su, X.; Zhu, Z.; Gao, W.-Y.; Wang, B.; Yin, A.-X. Promoting the Electrocatalytic Reduction of CO_2 on Ultrathin Porous Bismuth Nanosheets with Tunable Surface-Active Sites and Local PH Environments. *ACS Appl. Mater. Interfaces* **2022**, *14* (8), 10648−10655.

(49) Chen, L.; Hao, Y.; Li, J.; Hu, L.; Zuo, X.; Dai, C.; Yu, Z.; Huang, H.; Tian, W.; Liu, D.; Chang, X.; Li, P.; Shao, R.; Wang, B.; Yin, A. Controllable Crystallization of Two-Dimensional Bi Nanocrystals with Morphology-Boosted CO_2 Electroreduction in Wide PH Environments. *Small* **2023**, *19* (34), 1−9.

(50) Li, Z.; Sun, B.; Xiao, D.; Wang, Z.; Liu, Y.; Zheng, Z.; Wang, P.; Dai, Y.; Cheng, H.; Huang, B. Electron-Rich Bi Nanosheets Promote $CO_2^{\cdot -}$ Formation for High-Performance and PH-Universal Electrocatalytic CO_2 Reduction. *Angew. Chem., Int. Ed.* **2023**, *62* (11), No. e202217569.